Origin of Orientation Phenomena Observed in Layered Langmuir–Blodgett Structures of Hairy-Rod Polymers

Stefan Schwiegk,† Thomas Vahlenkamp,† Yuanze Xu,‡ and Gerhard Wegner*,†

Max-Planck-Institut für Polymerforschung, Postfach 3148, D-6500 Mainz, Germany, and Chinese Academy of Science, Institute of Chemistry, P.O. Box 2709, 100080 Beijing, China

Received August 22, 1991; Revised Manuscript Received December 10, 1991

ABSTRACT: The main chain orientation of polymers of the hairy-rod type in layered assemblies obtained by the Langmuir–Blodgett (LB) process has been investigated. The alignment of the transferred molecules parallel to the dipping direction is determined by the geometric conditions of the monolayer flow on the water subphase. Orientation due to the force field at the meniscus is negligible. Experimental data obtained for poly(tetramethoxytetraoctoxyphthalocyaninato)siloxane (PcPS), poly(γ-methyl L-glutamate)-*co*-(γ-*n*-octadecyl L-glutamate) (PG), isopentylcellulose (i-PC), and *n*-butylcellulose (n-BC) are theoretically analyzed in terms of the rheology of a two-dimensional liquid. The order parameter describing the degree of orientation of the backbones with regard to the dipping direction can be improved by annealing. This process obeys the time–temperature superposition principle.

1. Introduction

Gorter and Grendel[1] seem to be the first to have observed in 1925 the formation of a monomolecular film of macromolecules (proteins) on the water surface. It took several decades, however, before polymers at the air–water interface became a matter of greater interest because they are prerequisite to application of the so-called Langmuir–Blodgett (LB) technique.[2-4]

Our approach to this field is to use nonamphiphilic rigid-rod polymers dressed with flexible side chains.[5,6] It has been shown for several types of these hairy-rod polymers that they form a densely packed monolayer when spread to the air–water interface of a Langmuir trough. It was hinted that the packing within the monolayers is best described in terms of a two-dimensional liquid-crystalline (LC) phase. This two-dimensional LC phase becomes oriented in the course of the LB transfer process such that highly anisotropic layered assemblies are obtained.[7]

Supramolecular structures with a defined main chain orientation within each monolayer have been designed by utilizing these systems.[8] The applications of these anisotropic LB films in molecular optics and electronics are promising.[3,9,10]

Compared to the efforts spent to create and apply polymeric LB multilayers the knowledge about the origin of main chain orientation during the LB film assembly technique and the relations between the process parameters and the corresponding film structure is poor.

The investigation of the main chain orientation process touches on several fundamental problems, such as the fluid dynamics of rigid-rod polymers on the water surface, the macromolecular orientation in a two-dimensional flow, the possibility of stress-induced orientation at the meniscus, as well as the further orientation within the deposited multilayers in terms of relaxation processes.

This paper reports on the experimental observation and theoretical analysis of phenomena leading to the orientation of hairy-rod type polymers in the LB technique. The two-dimensional flow patterns have been determined and correlated with the macroscopic orientation in the transferred film, the influence of the meniscus on the main-chain orientation has been estimated, and the postorientation process on the substrate has been studied.

The following kinds of rigid-rod polymers have been investigated: poly(tetramethoxytetraoctoxyphthalocyaninato)siloxane (PcPS),[11] poly(γ-methyl L-glutamate)-*co*-(γ-*n*-octadecyl L-glutamate) (PG),[12] isopentylcellulose (i-PC), and *n*-butylcellulose (n-BC).[13] All polymers are quite soluble in organic solvents. They exhibit good LB film-forming and transfer characteristics, which include a high collapse pressure, a fast drainage speed, and a quantitative transfer ratio.

2. Flow and Deformation of a Monolayer on the Water Surface

2.1. Hydrodynamic Considerations. Using the LB technology for designing mono- or multilayered structures implies the formation of a densely packed monolayer at the air–water interface and the transfer of this monolayer by dipping and raising of a substrate through the interface under a constant surface pressure.

In this process the transfer of the molecules induces a flow of the monolayer on the water surface. If the drag of the water on the monolayer is neglected, the flow can be described in terms of a two-dimensional problem of fluid mechanics. With this assumption in mind a mathematical analysis using the model of an ideal fluid will be presented as a first approximation of the flow of a monolayer. Effects due to the nature of the rigid-rod molecules will then be discussed next.

2.1.1. Ideal Fluid. Generally, the two-dimensional creeping flow of an ideal fluid can be expressed by a complex potential:

$$\omega = \Phi + i\psi \tag{2.1}$$

where the potential function Φ = const defines the equipotential lines and the stream function Ψ = const defines the streamlines. The potential function can be obtained by solving the Laplace equation:

$$\nabla^2\Phi = \frac{\partial^2\Phi}{\partial x^2} + \frac{\partial^2\Phi}{\partial y^2} = 0 \tag{2.2}$$

The analytical solution has already been demonstrated under the following assumptions:[14] First, the substrate is represented by a finite line sink, and second, the trough is regarded as infinite in its dimensions.

† Max-Planck-Institut für Polymerforschung.
‡ Chinese Academy of Science.

0024-9297/92/2225-2513$03.00/0

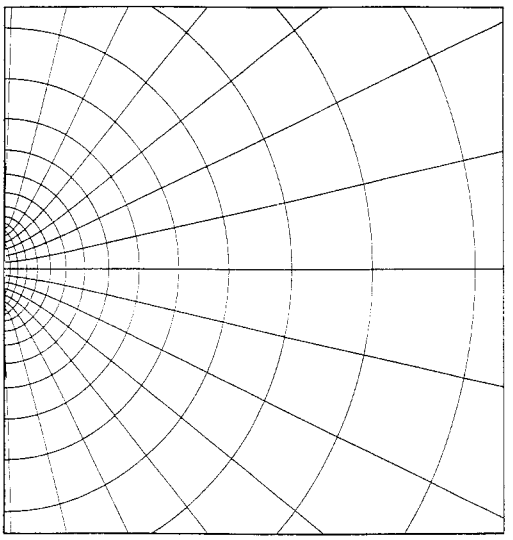

Figure 1. Calculated streamlines (Ψ = const) and equipotential lines (Φ = const) for the two-dimensional ideal fluid in a trough with infinite dimensions: sink width 26 mm.

Assuming a finite line sink means that the thickness of the substrate is neglected and that the transfer of the monolayer proceeds without any meniscus, while complications from boundary conditions can be avoided by assuming infinite trough dimensions.

The analytical solutions for Φ and Ψ have been obtained by integrating the equation for the complex velocity potential:[15]

$$\omega(z) = \frac{m}{a}\int_{-a/2}^{a/2} \ln (z - y')\, dy' \tag{2.3}$$

where $z = y + ix$, a is the width of the substrate, and m/a is the scaling "magnitude per unit length".

The resulting expressions for Φ and Ψ are

$$\Phi = \frac{m}{2a}\left[\left(y+\frac{a}{2}\right)\ln\left\{x^2+\left(y+\frac{a}{2}\right)^2\right\}-\left(y-\frac{a}{2}\right)\ln\left\{x^2+\left(y-\frac{a}{2}\right)^2\right\}+2x\left\{\arctan\left(\frac{y+\frac{a}{2}}{|x|}\right)-\arctan\left(\frac{y-\frac{a}{2}}{|x|}\right)\right\}\right] \tag{2.4}$$

$$\Psi = \frac{m}{2a}\left[-2\left(y+\frac{a}{2}\right)\arctan\left\{\frac{y+\frac{a}{2}}{x}\right\}+2\left(y-\frac{a}{2}\right)\arctan\left\{\frac{y-\frac{a}{2}}{x}\right\}+x\ln\left\{x^2+\left(y+\frac{a}{2}\right)^2\right\}-x\ln\left\{x^2+\left(y-\frac{a}{2}\right)^2\right\}\right] \tag{2.5}$$

The equipotential lines and the streamlines for Φ = const and Ψ = const, respectively, are shown in Figure 1.

For the trough geometry under investigation (see Figure 2a) the flow field has been determined for "film deposition" only onto the side of the substrate facing the moving barrier. In this case the boundary problem can be defined in the rectangular coordinate system as follows (Figure 2a):

side 1

$$v_x = \frac{\partial\Phi}{\partial x} = -v_b = \text{const} \tag{2.6a}$$

where v_x is the x-component of the velocity and v_b is the velocity of the moving barrier.

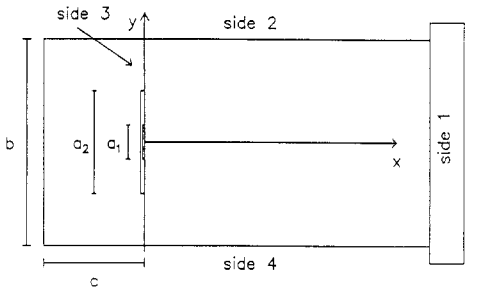

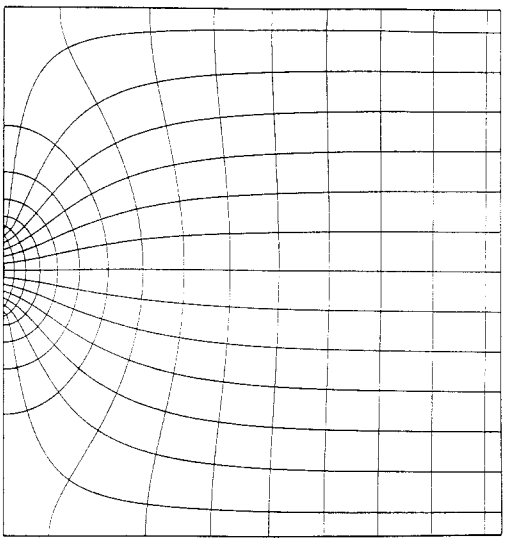

Figure 2. (a, top) Geometry of the real trough: side 1 moving barrier, side 3 boundary defined by the position of the substrate; a_1 (=26 mm) and a_2 (=75 mm) indicate the width of two different substrates; b = 150 mm; c = 75 mm. The x- and y-axes define the coordinate system. (b, bottom) Numerically calculated equipotential and streamlines for the ideal fluid in the real trough (for one-sided "deposition"): sink width 26 mm; trough width 150 mm.

side 2/4

$$v_y = \frac{\partial\Phi}{\partial y} = 0 \tag{2.6b}$$

where v_y is the y-component of the velocity; both sides are equal according to symmetry.

side 3

$$v_{x}\big|_{\substack{x=0\\ y\le a/2}} = -v_d \qquad v_{x}\big|_{\substack{x=0\\ a/2<y<b/2}} = 0 \qquad v_d = \frac{b}{a}v_b \tag{2.6c}$$

where v_d is the dipping velocity (transfer velocity) and a and b are defined in Figure 2a.

With these boundary conditions the Laplace eq 2.2 has been solved numerically using a so-called "fast Poisson solver based on the HODIE finite difference scheme on a uniform mesh".[16]

Successively the stream function has been calculated by numerical differentiation and following integration of the potential function according to eq 2.7 and eq 2.8, respectively.

$$v_x = \frac{\partial\Phi}{\partial x} = \frac{\partial\Psi}{\partial y} \qquad v_y = \frac{\partial\Phi}{\partial y} = -\frac{\partial\Psi}{\partial x} \tag{2.7}$$

$$\Psi = \frac{1}{2}\left[\int_0^y \frac{\partial\Phi}{\partial x}\,dy - \int_0^x \frac{\partial\Phi}{\partial y}\,dx\right] \tag{2.8}$$

The resulting equipotential lines and streamlines are shown in Figure 2b. As expected, they are perpendicular to each other, indicating that the numerical solution is good.

Comparing Figure 1 and Figure 2b, it is obvious that both solutions coincide well in the region near the substrate and the effect of the trough geometry can be neglected. This in turn indicates the working range of the analytical solutions.

It should be mentioned that all the kinematic quantities, e.g., the velocity and the velocity gradient, are defined by the potential function as shown in eq 2.6 a–c, eq 2.9, and eq 2.10, where the velocity gradient tensor **F** equals

$$\mathbf{F} = \begin{vmatrix} \frac{\partial v_x}{\partial x} & \frac{\partial v_y}{\partial x} \\ \frac{\partial v_x}{\partial y} & \frac{\partial v_y}{\partial y} \end{vmatrix} = \begin{vmatrix} \Phi_{xx} & \Phi_{xy} \\ \Phi_{yx} & \Phi_{yy} \end{vmatrix} \tag{2.9}$$

and the deformation rate tensor **D** equals

$$\mathbf{D} = \begin{vmatrix} \Phi_{xx} & 1/2(\Phi_{xy} + \Phi_{yx}) \\ 1/2(\Phi_{xy} + \Phi_{yx}) & \Phi_{yy} \end{vmatrix} \tag{2.10}$$

For an ideal fluid there is $\Phi_{xx} = -\Phi_{yy}$ and $\Phi_{xy} = \Phi_{yx}$ and therefore

$$\mathbf{F} = \mathbf{D} \tag{2.11}$$

In addition, a coordinate invariant scalar parameter G to describe the deformation rate can be introduced:

$$G = \sqrt{\frac{J}{2}} = \sqrt{\frac{1}{2}\,\mathrm{tr}\,\mathbf{D}^2} = \sqrt{\Phi_{xx}^2 + \Phi_{xy}^2} \tag{2.12}$$

where J is the second invariant of the tensor **D** and tr means the trace.

The calculated values of v_x and G are schematically shown in Figure 3, parts a and b, respectively. Obviously the deformation is concentrated near the substrate for the ideal fluid.

2.1.2. Kinematics of Other Fluid Models. Concerning a compressed monolayer consisting of rigid-rod molecules, the assumption of zero viscosity as for the ideal fluid is of course a rough approximation. Therefore, the flow patterns of other kinds of fluids should be regarded as well.

The rheological behavior of various types of fluids has been studied under the condition of a plane channel flow through an abrupt contraction in terms of a two-dimensional problem. The agreement of the numerically calculated flow fields and those observed experimentally is satisfying for both Newtonian and non-Newtonian fluids.[17]

The calculated streamlines of a two-dimensional creeping flow into a rectangular contraction of one-quarter of the channel width are shown in Figure 4 for an ideal fluid (a), a Newtonian fluid (b),[17] and a viscoelastic fluid (Johnson–Segalman fluid) (c).[18] For an ideal fluid the stream function changes its value linearly across the channel, while for viscous fluids the streamlines tend to leave the channel center. This implies a larger velocity gradient across the channel for viscous fluids.

The highly viscoelastic fluid (Figure 4c), which is modeled by a Johnson–Segalman fluid with a single relaxation time, shows recirculations at the corner. The recirculation pattern agrees with the experimental observation using highly viscoelastic fluids. The vortices become larger when the Weissenberg number We = $T_{11} - T_{22}/2T_{12}$ increases, which is defined as the ratio of the first normal stress difference (elasticity) to shear stress (viscosity).

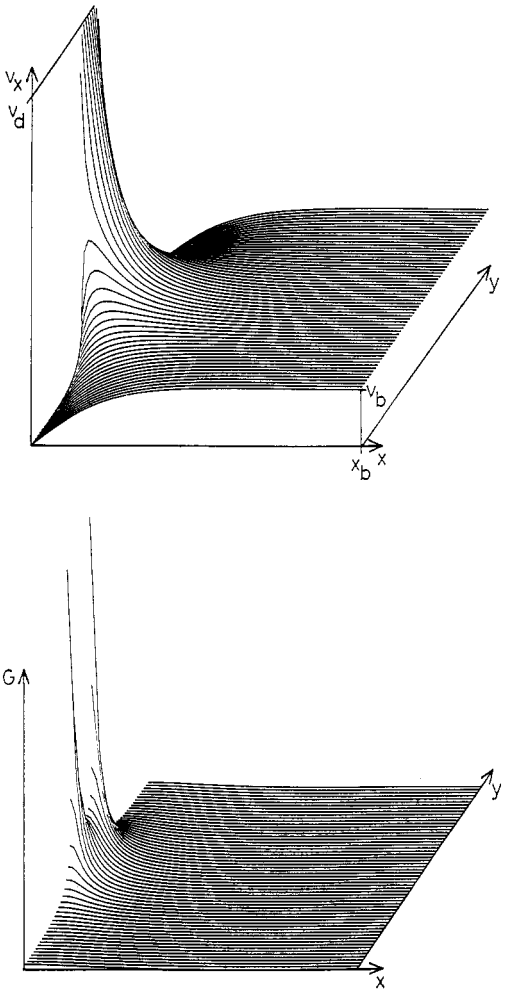

Figure 3. (a, top) Calculated velocity distribution of v_x for the ideal fluid in the real trough: sink width 26 mm; trough width 150 mm; v_d dipping velocity; x_b moving barrier position; v_b barrier velocity. (b, bottom) Calculated deformation rate G for the ideal fluid in the real trough: sink width 26 mm; trough width 150 mm.

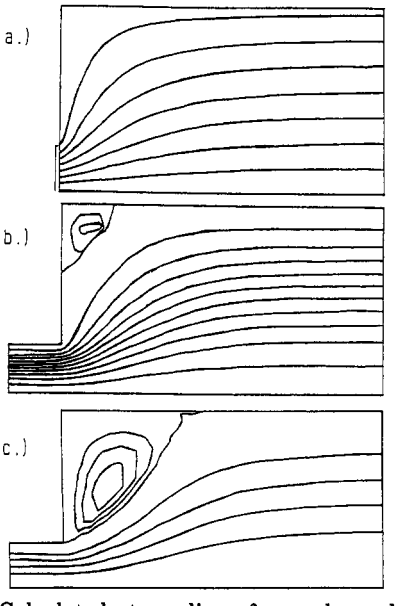

Figure 4. Calculated streamlines for a plane channel flow through an abrupt contraction of one-quarter of the channel width for an ideal fluid (a), a Newtonian fluid (b), and a highly viscoelastic fluid (c). Closed streamlines indicate recirculation areas.

The angle which separates the flowing out region from the recirculation regions is called the convergent angle.

Table I
Some Structural and LB Properties of the Investigated Polymers

	polymer			
	PcPS	PG	i-PC	n-BC
chemical structure	Figure 13	Figure 14	Figure 15	Figure 15
degree of polym, P_w	30–100	500–1000	270	270
rod length, Å	100–500	750–1500	1400	1400
persistence length, Å	infinite[a]	500–1000	~60[19]	~60[19]
spreading concn, mg/mL of $CHCl_3$	1–2	0.3	0.7	0.7
subphase temp, °C	6–10	20	10–20	11
collapse pressure, mN/m	40	25–30	20	18
working pressure, mN/m	15–25	19–22	15	12
max deposition speed, cm/min	>3	>6	>1	>1

[a] Greater than rod length.

Its value decreases from 180° for the ideal fluid to ~90° for the viscoelastic fluid in Figure 4c.

It should be remarked that the numerical calculations for Figure 4b and c have been obtained under the boundary conditions that the upstream is a fully developed flow and that there is no slip at the channel wall. It will be seen later from the experiments that these conditions are not well satisfied for the rigid-rod polymer systems under investigation.

2.2. Experimental Determination of the Flow Field for Polymeric Monolayers. 2.2.1. Polymer Samples. Table I summarizes structural informations and the characteristic LB data for the three types of polymers: poly(tetramethoxytetraoctoxyphthalocyaninato)siloxane (PcPS),[11] poly(γ-methyl L-glutamate)-*co*-(γ-*n*-octadecyl L-glutamate) (PG),[12] and the cellulose ethers isopentylcellulose (i-PC) and *n*-butylcellulose (n-BC).[13]

2.2.2. Flow Visualization during LB Film Transfer. There are several methods which allow the visualization of the flow field in a LB trough.[20,21] The choice is restricted due to the condition that flow visualization combined with an undisturbed film transfer must be achieved. Therefore, the flow fields have been determined applying a method suggested by Daniel.[21] Visualization was realized by cleaned aluminium disks (diameter 2–4 mm, thickness 0.01 mm), which were positioned on top of the compressed monolayer using clean tweezers. The positions of the floating disks were recorded by a camera, mounted vertically above the LB trough. The film transfer was carried out under constant pressure using an automatic Lauda film balance. When individual disks arrived near the substrate, they were removed in order to allow the recovery of the film before deposition. The transfer ratio was kept near 100%, and subsequently the LB film covered substrate was used to determine the main chain orientation.

For the investigated transfer geometry, the streamlines have been obtained by successive projections of the recorded slides. Successive slides visualize the movement of the disks, while corresponding positions map their trajectories. Assuming that the movement of the disks is representative for the film flow, the streamlines have been determined. This process is schematically drawn in Figure 5, where the black points correspond to the initial positions.

Different transfer geometries as indicated in Figure 6 a–d give rise to different flow patterns. The corresponding main chain orientations are discussed in section 3.2.

In section 2.1.1 the theoretical streamlines for the "deposition" of an ideal fluid only onto the side facing the moving barrier have been discussed. This condition has been realized experimentally using a substrate holder made of Teflon, where the substrate slides within a notch

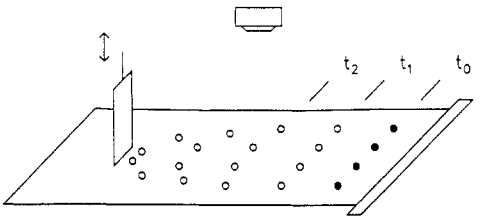

Figure 5. Experimental detection of the streamlines during LB film transfer (schematically). Black points correspond to the initial positions of the aluminium disks used for flow visualization.

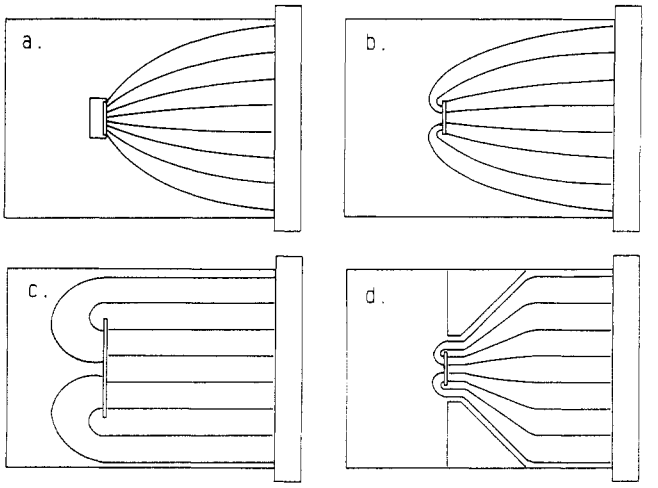

Figure 6. Investigated transfer geometries and observed streamlines (schematically).

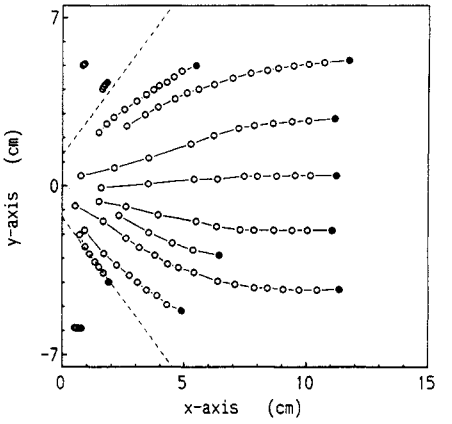

Figure 7. Streamlines for the transfer of PcPS only onto the substrate side facing the moving barrier: substrate width 26 mm; T = 6 °C; π = 25 mN/m; v_d = 1 cm/min. Dashed lines indicate the sides of the convergent angle of ~110°.

shielding the back side from film deposition (see Figure 6a). In this case, the boundary conditions are similar to the problem of a sink flow unless there is no wall of the trough at both edges of the substrate.

The directly measured flow patterns will be compared with those predicted by various fluid models. (see section 2.3.)

2.2.3. Flow Patterns during Transfer. 2.2.3.1. PcPS. The streamlines for the one-sided transfer of PcPS onto a substrate having a width of 2.6 cm are shown in Figure 7. Far from the substrate they are parallel to each other and the disks move with the same velocity as the moving barrier. This indicates that there is no viscous drag at the wall of the trough, a behavior similar to the boundary condition for the ideal fluid. But it has to be mentioned that this result is limited to the experimentally realized distance between disks and the trough boundary of ~0.5 cm.

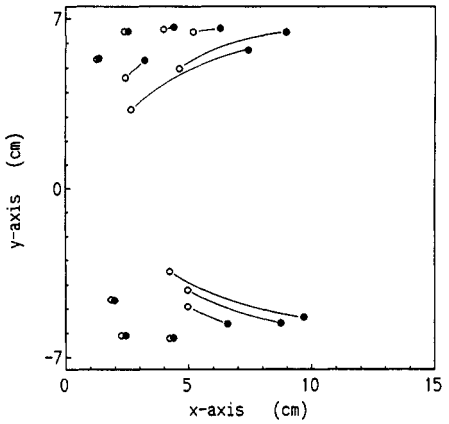

Figure 8. Initial and final positions of some indicator disks linked by the corresponding streamlines for the one-sided transfer of PcPS: substrate width 26 mm; T = 6 °C; π = 25 mN/m; v_d = 1 cm/min.

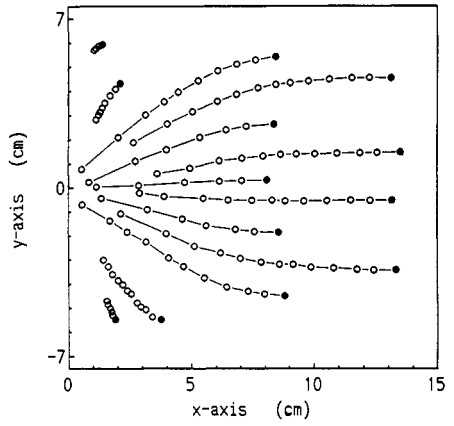

Figure 9. Streamlines for the one-sided transfer of PG: substrate width 26 mm; T = 20 °C; π = 19 mN/m; v_d = 1 cm/min.

Near the transfer region the flow becomes convergent like a sink flow. It is worth noting that there is a convergent angle at the center leaving two areas, in which the monolayer is almost at rest. This detail is stressed in Figure 8, where in another experiment the initial and the final positions of the disks are linked by the streamlines. The convergent angle of ~110° seems to be insensitive to the flow rate. A velocity profile is developed having its maximum in the center and a drastic velocity gradient at both sides near the convergent angle and leaving undeformed areas at both corners. This behavior is supposedly viscoplastic in its nature, but an exact solution for this boundary problem is not available to us.[22]

2.2.3.2. PG. The flow pattern of PG is very similar to that of PcPS as shown in Figure 9. Only a little increased mobility of the monofilm has been detected in the corners. This may be related to the somewhat reduced rigidity of the polymer chains in PG or to the effect of the higher subphase temperature in the experiments performed with PG. More exactly the term "reduced temperature" should be used, which could be defined as the ratio of the temperature during the experiment to the temperature at which no stable monolayer is formed when applying the same surface pressure. Unfortunately, this temperature cannot be determined due to experimental restrictions.

2.2.3.3. Cellulose Ethers. i-PC and n-BC monofilms exhibit a higher mobility as visualized in their flow patterns in Figure 10a and b. Due to the enhanced fluidity of the film, small perturbations may cause irregular motion of the indicator disks. A remarkable feature has been found for n-BC, revealing that there exist recirculations at both

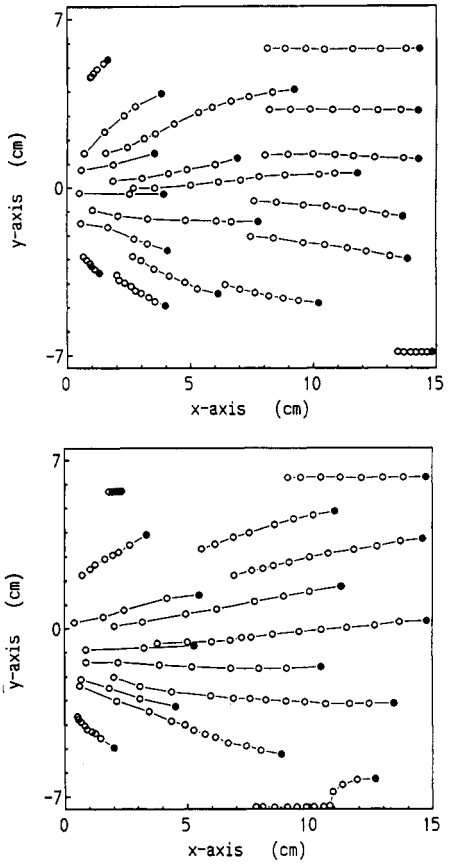

Figure 10. (a, top) Streamlines for the one-sided transfer of i-PC: substrate width 26 mm; T = 10 °C; π = 13 mN/m; v_d = 1 cm/min. (b, bottom) Streamlines for the one-sided transfer of n-BC: substrate width 26 mm; T = 10 °C; π = 10 mN/m; v_d = 1 cm/min.

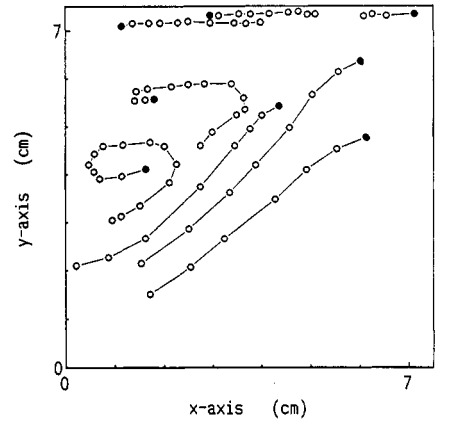

Figure 11. Streamlines in one edge of the trough near the substrate for the one-sided transfer of n-BC: substrate width 26 mm; T = 10 °C; π = 10 mN/m; v_d = 1 cm/min.

edges of the substrate; i.e., the disks near the wall move back toward the main stream, which is shown in detail in Figure 11. These vortices are similar to the vortices in the sink flow of highly viscoelastic fluids.[22,23] Therefore this new phenomenon of the in-plane flow of monolayers may also be related to a viscoelastic behavior of cellulose ethers.

2.3. Modeling of the Surface Flow of Polymeric Monolayers. As far as the kinematic behavior of surface flow for the polymers under investigation is concerned, it has to be admitted that the ideal fluid model provides only a rough approximation. For example, the convergent angle is in the range of 110° compared to 180° for the ideal fluid. More quantitative estimations of the deformation rate and the deformation field need a more realistic rheo-

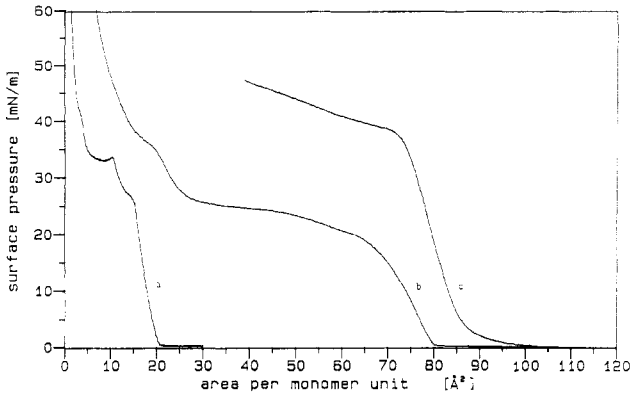

Figure 12. π/A isotherms for PG (a, T = 20 °C), n-BC (b, T = 20 °C), and PcPS (c, T = 6 °C).

logical modeling.

Some physical considerations would be helpful here. It has long been known that rodlike polymers in concentrated solutions form a liquid-crystalline, nematic phase. It has also been proposed that rodlike polymers with side chains form a nematic phase in solution as well as in the molten state. However, the question of whether on the water surface, where the interfacial thermodynamic conditions are quite different from those in bulk, the compressed monolayers of these polymers are also in the nematic state still needs direct proof.

The π/A isotherms of the polymers under consideration are shown in Figure 12. First, the area per monomer unit, where the flow experiments have been performed, reflects the density of a closely packed monolayer. Second, the isotherms are reversible until the collapse pressure (the first plateau) is reached. These facts may support a continuous monolayer with weak interactions between the molecules. Moreover, the fact that the densely packed molecules lubricated by flexible side chains retain good fluidity also strengthens the assumption that they may flow like a two-dimensional liquid crystal. Polymers of higher rigidity like PcPS and PG should exhibit a behavior more akin to nematic systems,[24-26] e.g., plastic yield behavior under stress. More flexible polymers like the cellulose ethers feature a more viscoelastic behavior, e.g., the wall vortices as in the case of three-dimensional rheology.[17,27]

Further work in modeling the flow of monolayers should involve two tasks; first, to develop the rheological model adequate for monolayers under large deformation and complex flow and, second, to calculate the boundary problem with more realistic boundary conditions, e.g., allowing slip at the wall.

3. Deformation-Induced Main Chain Orientation

3.1. Measurement of Main Chain Orientation. For PcPS and PG the molecular orientation has been determined in the transferred film. Spectroscopy in the visible region is very suitable for PcPS due to the strong phthalocyanine absorption. This so-called Q-band is shifted from λ_{max} = 680 nm in the monomer to λ_{max} = 545 nm in the polymer arising from the coupled electronic transitions of neighboring chromophores.[28] The dipole transition moment lies within the plane of the phthalocyanine chromophore, perpendicular to the polymer backbone (see Figure 13). Therefore, strong absorption is observed, if the incident light is polarized perpendicular to the backbone. The polarized visible spectrum for a highly ordered LB film is shown in Figure 13. $A_\perp$ and $A_\parallel$ are the absorptions measured perpendicular and parallel to the

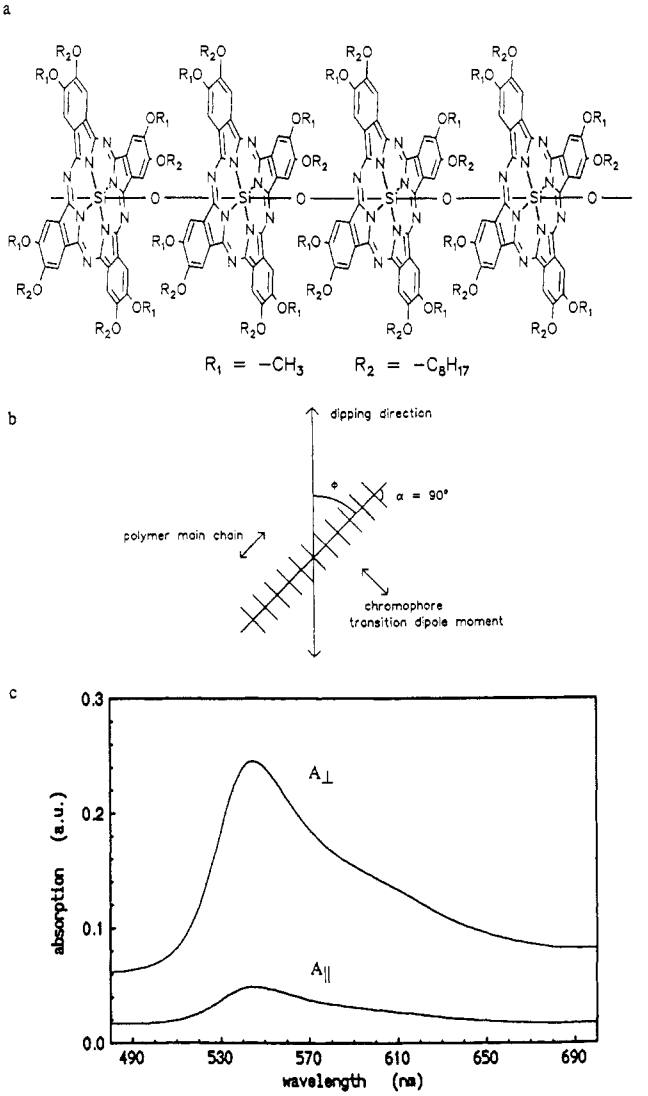

Figure 13. Molecular structure of PcPS (a), evaluation of the main chain orientation by the known transition dipole moment of the chromophore (b), and absorption of a film of 40 layers in polarized visible spectroscopy (c): $A_\perp$ absorption, when the incident beam is polarized perpendicular to the dipping direction.

dipping direction. The degree of orientation is characterized by the dichroic ratio R:

$$R = A_\perp/A_\parallel \tag{3.1}$$

The polarized visible spectrum (Figure 13) has been measured for a PcPS film of 40 monolayers. This implies that only an averaged orientation is obtained. For the investigation of the orientation process, it was desirable to determine the absorptions $A_\perp$ and $A_\parallel$ in a single monolayer. Due to noise and baseline shift it was necessary to analyze the whole Q-band, assuming that the dichroic ratio is independent of the wavelength. Therefore eq 3.1 was extended:

$$R = \frac{(A_\perp)_i - a}{(A_\parallel)_i - b} \qquad i = 1, 2, ..., n \tag{3.2}$$

where $(A_\perp)_i$ and $(A_\parallel)_i$ are the absorptions measured at the ith wavenumber based on the given baselines, respectively. The unknown values a and b are the differences between the given baselines and the true baseline. Therefore, it is

$$(A_\perp)_i = R(A_\parallel)_i + (a - Rb) \tag{3.3}$$

The linear regression of eq 3.3 enables the exact deter-

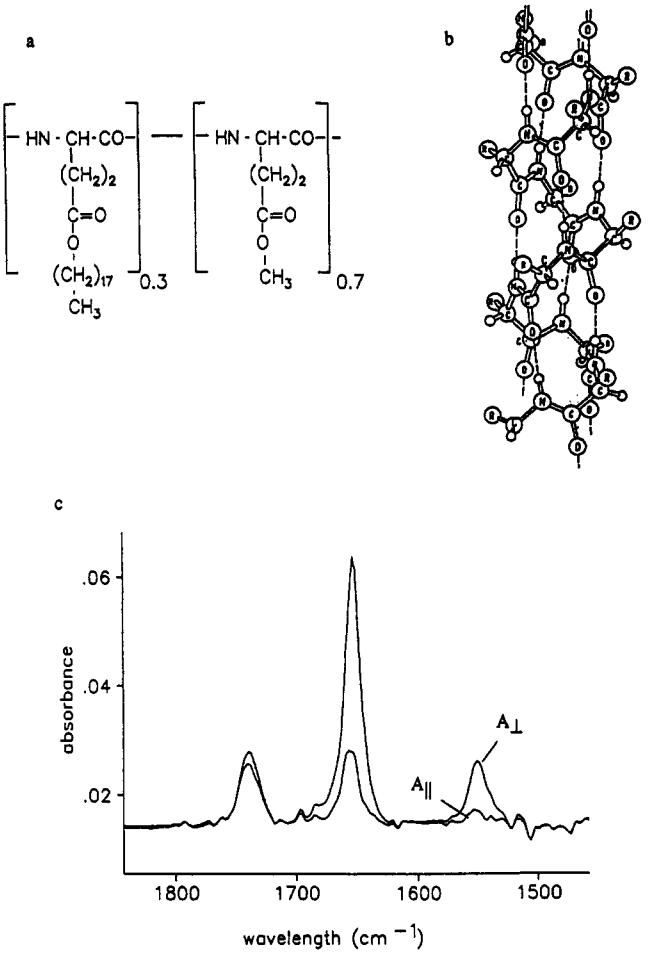

Figure 14. Averaged composition of repeat units (a) and helical structure (b) of PG and part of the polarized IR spectra of a film of 40 layers on a silicon substrate (region of amide bands) (c).

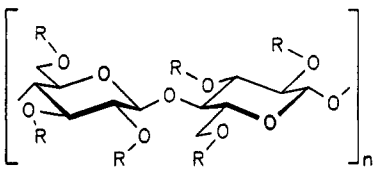

Figure 15. Structure of the cellulose ethers i-PC (R = *i*-C_5H_{11}) and n-BC (R = *n*-C_4H_9).

mination of R values even for a monofilm. Effects due to reflectivity losses in the determination of the dichroic ratio were estimated to be negligible.

For PG multilayers the orientation has been determined using polarized FTIR spectroscopy.[6] The glutamate repeat units arrange in a helical conformation, due to hydrogen bonds. Therefore, PG is a cylindrical molecule. The dichroic ratio has been calculated according to ref 29, using the absorption at 1550 cm^{-1} due to the amide bond oscillation (Figure 14).

The orientation of rodlike polymers lying in a plane defined by the substrate surface can be described by the two-dimensional order parameter S of a nematic phase:[30]

$$S = \langle \cos 2\Phi \rangle = \int_0^{\pi} f(\Phi) \cos 2\Phi \, d\Phi \qquad (3.4)$$

where $f(\Phi)$ is the normalized distribution function of the main chain orientation, i.e., the probability of a molecule to be oriented with an angle Φ to the main direction. For simplicity, the latter direction is chosen as the average direction of the distribution.

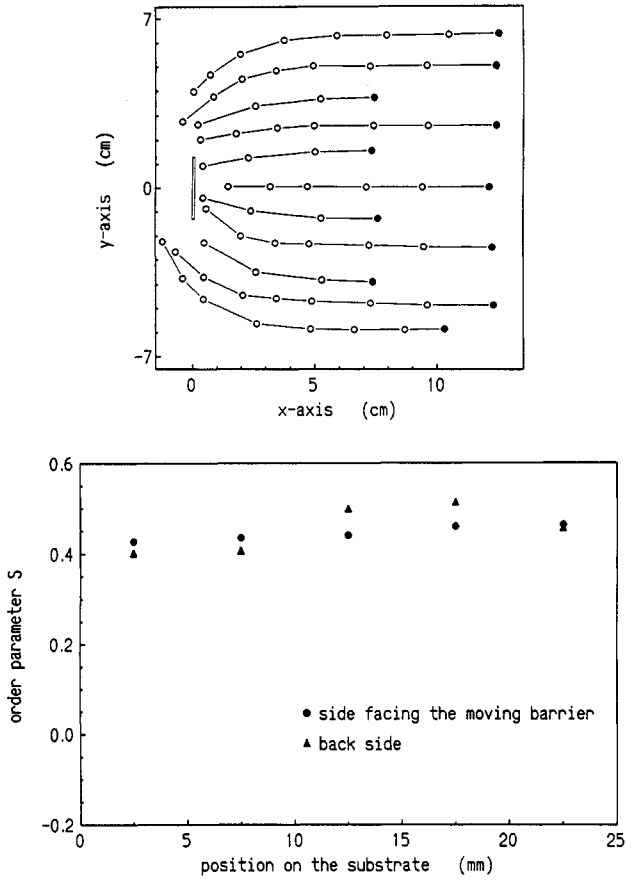

Figure 16. (a, top) Streamlines for the two-sided transfer of PcPS: substrate width 26 mm; T = 6 °C; π = 25 mN/m; v_d = 1 cm/min. (b, bottom) Order parameter S of the deposited multilayers of PcPS versus the horizontal position on the substrate for the transfer described in (a).

The order parameter can be calculated from the dichroic ratio:[8]

$$S = \frac{R-1}{R+1}(1 - 2\cos^2 \alpha) \qquad (3.5)$$

The definition of α is indicated in Figure 13.

3.2. Main Chain Orientation after Different Flow Histories. For a better understanding of the main chain orientation the following experiments have been designed to correlate the flow pattern with the macroscopic orientation.

3.2.1. Effect of the Substrate Width. The flow pattern during the two-sided transfer process of PcPS on a substrate having a width of 2.6 cm is presented in Figure 16a. It was of interest to measure variations in the local orientation on the substrate along a line normal to the dipping direction. This measurement allows one to correlate the orientation of multilayers on the substrate with the flow conditions as visualized by the streamlines. The order parameter S is plotted versus the horizontal position on the substrate in Figure 16b, separately for the front side, which has faced the moving barrier, and the back side. The order parameter exceeds 0.4 for the front side, indicating that the molecules tend to orient parallel to the dipping direction.

If the width of the substrate equals half of the width of the trough, parallel streamlines should be generated in front of the substrate. This results from half of the monolayer flowing around the substrate and being deposited onto the back side (see Figure 17a). Therefore, the monolayer deposited on the front side has not faced any detectable flow deformation (For the effect of the meniscus,

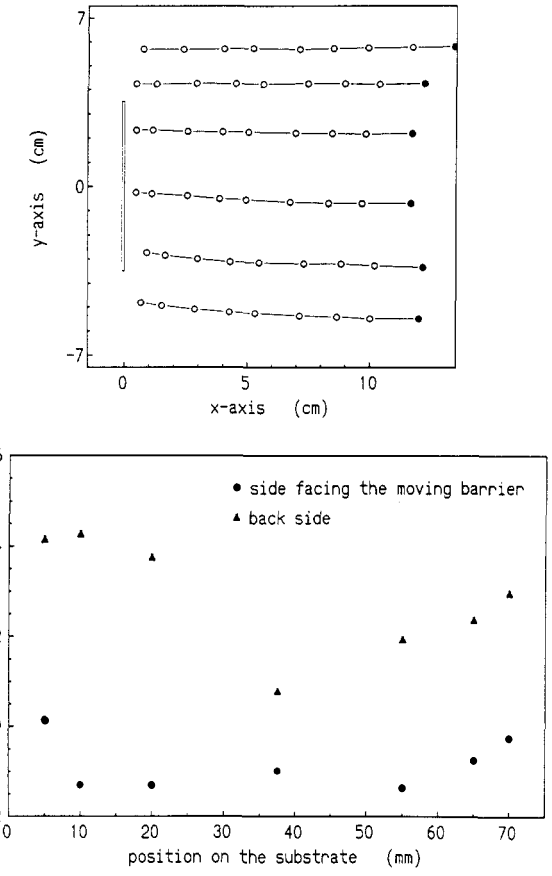

Figure 17. (a, top) Streamlines for the two-sided transfer of PcPS: substrate width 75 mm; T = 10 °C; π = 15 mN/m; v_d = 1 cm/min. (b, bottom) Order parameter S of a multilayer structure of PcPS versus the horizontal position on the substrate for the transfer described in (a).

see section 4.). The order parameter S is shown in Figure 17b for this geometry, separately for the front and the back sides. On the side that has faced the moving barrier there is no macroscopic orientation ($S \approx 0$). Actually, S values are a little less than zero, which may imply that the molecules in the compressed film have a weak orientation parallel to the substrate on the water surface. This may be caused by the deformation of the monolayer during compression.[31] The S values at the back side are larger than 0.3, especially at both edges of the substrate.

Investigations of poly[bis(*m*-butoxyphenyl)silane][32] and PG under similar flow conditions resulted in the same orientation characteristics.

These results indicate that a convergent flow, as it is developed for substrates less or equal in their width than one-fifth of the trough, is essential to obtain a main chain orientation of the polymer to be transferred to a substrate. Deposition of an undeformed monolayer as it is observed for substrates comparable in their width to half of the cross section of the trough will not lead to any significant orientation.

It is worth mentioning that Ogawa et al.[33] observed increasing orientation for copper phthalocyanine derivatives when they decreased the substrate width.

3.2.2. Convergent Channel Geometry. In order to prove the role of a converging flow for the molecular orientation, a transfer position after a 90° conical channel has been investigated, as shown in Figure 18. Again a substrate having half of the width of the channel was used for deposition but after a converging zone. In this case the transferred film shows an order parameter of ~0.4, differing from the random orientation without converging

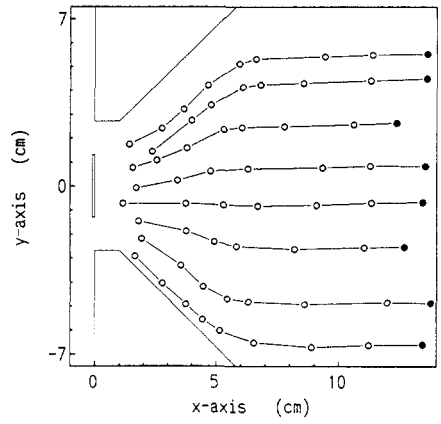

Figure 18. Streamlines for the two-sided transfer of PcPS applying a conical channel: substrate width 26 mm; channel width 54 mm; T = 6 °C; π = 25 mN/m; v_d = 1 cm/min.

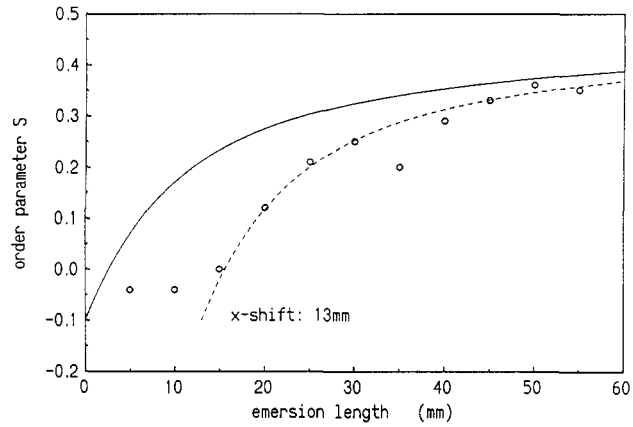

Figure 19. Order parameter S as a function of the emersion length of a substrate for the two-sided transfer of PcPS: substrate width 26 mm; T = 6 °C; π = 20 mN/m; v_d = 1 cm/min; circles, experimental results for the side facing the moving barrier; solid line, theoretical estimation; dashed line, x-shifted fit.

flow, but similar to the one found for the natural convergent angle in Figure 16a.

3.2.3. Orientation Change during a Single Monolayer Deposition. The evolution of orientation in the surface layer has been demonstrated by the transfer of a single monolayer. The 2.6-cm-wide substrate was immersed under the water surface of the trough before spreading and compression of the monolayer. Then the monolayer was transferred by the emersion process. By measuring the dichroic ratio from the first deposited area (upper part of the substrate) successively to the last deposited area (substrate bottom), it has been found that the molecules deposited in the first area are randomly oriented and that for successive areas their orientation increases gradually to a stationary value, as shown in Figure 19. The same experiment with a substrate having a width of 7.5 cm reveals no orientation development.

It was also proved that the relaxation of the orientation on the water subphase is slow. If the monolayer deposition is made with a 1-, 3-, or 10-min delay time between successive areas, where the dichroic ratio is measured, the orientation develops not much differently from Figure 19. Moreover, the orientation in the surface layer at the dipping position can be preserved until the next monolayer is transferred onto a new substrate by immersion.

Therefore, it can be concluded that the deformation of the surface layer is responsible for the orientation of the deposited film. Furthermore, the macroscopic orientation is correlated to the total deformation a plane element on

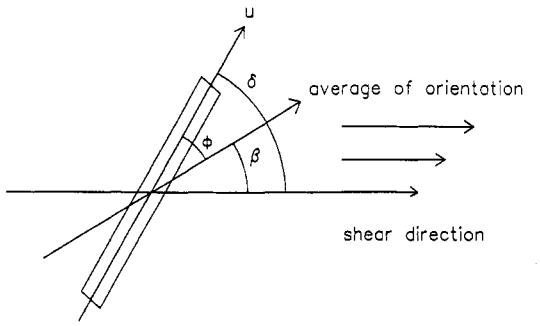

Figure 20. Definition of the unit vector **u** of a "test rod" and of the average of the orientation distribution with respect to the shear direction.

the water surface has suffered. Here the term "deformation induced" should be used rather than "flow induced", for it is the deformation rather than the movement or flow rate which dominates the orientation in the monolayer.

3.3. Mechanism of Macromolecular Orientation. If the macroscopic orientation can be described by the microscopic arrangement of the molecules during deformation, it would be reasonable to treat the monolayer flow in terms of the rheology of rodlike particles in the nematic phase.

A well-known molecular theory dealing with the dynamics of liquid-crystal polymers in concentrated solutions is the one presented by Doi.[34] Recently, Marrucci and Maffettone have analyzed the corresponding two-dimensional problem.[30]

The theory assumes that the nematic state can be described by a potential of the Maier–Saupe type:

$$V(\mathbf{u}) = -2Uk_BT\langle\mathbf{uu}\rangle:\mathbf{uu} \tag{3.6}$$

where U is the nondimensional intensity of the potential, $\mathbf{u} = (\cos\delta, \sin\delta)$ is the unit vector parallel to the "test rod" in the plane with an angle δ between the long axis of the rod and the shear direction, and $\langle\ \rangle$ indicates the average over the existing **u** distribution (Figure 20).

A shear flow results in a rotation of a thin rod with an angular velocity given by

$$\dot{\delta} = -G\sin^2\delta \tag{3.7}$$

where G is defined in eq 2.12. In a complex flow this deformation rate has to be multiplied by a flow field correction factor m due to the fact that shear and elongation components are present.

The molecular orientation can be described by the diffusion equation

$$\frac{df}{dt} = -\frac{\partial J}{\partial\delta} \tag{3.8}$$

According to ref 30, the angular flux of rods is written as

$$J = -D\left[\frac{\partial f}{\partial\delta} + \frac{f}{k_BT}\frac{\partial V}{\partial\delta}\right] + \dot{\delta}f \tag{3.9}$$

where D is a rotational diffusion coefficient.

Usually the solution of eq 3.8 is given for the stationary case; i.e., $df/dt = 0$.[14,30] This assumption seems not to be justified for the investigated systems due to the slow relaxation of the macroscopic orientation as discussed in section 3.2.3.

For this reason the transient solution of eq 3.8 in the limit case of negligible diffusion will be deduced. Then, combining eqs 3.8 and 3.9 results in

$$\frac{df}{dt} = -\frac{\partial}{\partial\delta}(\dot{\delta}f) \tag{3.10}$$

Using eq 3.10, the time-dependence of the order parameter S defined in eq 3.4 can be determined.

In a first step, eq 3.4 has to be differentiated with respect to the time t:

$$\frac{dS}{dt} = \int_0^\pi \frac{\partial f}{\partial t}\cos 2\Phi\, d\Phi - 2\int_0^\pi f\dot{\Phi}\sin 2\Phi\, d\Phi \tag{3.11}$$

To replace the angle δ in eq 3.10 with the angle Φ, a coordinate axis is chosen in the direction where $\beta = \delta - \Phi$ (see Figure 20). For a symmetric distribution function this provides

$$\langle\sin 2\Phi\rangle = 0 \qquad \langle\sin 4\Phi\rangle = 0 \tag{3.12}$$

By substituting eqs 3.10 into 3.11 and integrating by parts, eq 3.13 is obtained:

$$\frac{dS}{dt} = \frac{G}{2}\int_0^\pi (1-\sin^2 2\Phi)f\, d\Phi - \frac{G}{2}S \tag{3.13}$$

The distribution function for a two-dimensional nematic crystal can be written as[30]

$$f(\Phi) = C\exp(a\cos 2\Phi) \tag{3.14}$$

where $a = U\langle\cos 2\Phi\rangle$ and C is a constant given by the normalization condition. Using the definition of a and eq 3.14, an expression for U can be given:

$$\langle\sin^2 2\Phi\rangle = 1/U \tag{3.15}$$

A shear flow will change the main orientation direction, i.e., the skewness of the distribution and the value of $\langle\sin^2 2\Phi\rangle$, but not much if U or G values are large enough.[34]

Therefore, an approximate relationship for the orientation evolution can be obtained by substituting eqs 3.14 and 3.15 into eq 3.13:

$$\frac{dS}{dt} = \frac{G}{2}\left(\frac{U-1}{U} - S\right) \tag{3.16}$$

and after integration

$$S = \frac{U-1}{U}\left[1 - \left(1 - \frac{US_0}{U-1}\right)\exp\left(-\int_0^t \frac{G}{2}\,dt\right)\right] \tag{3.17}$$

$S = S_0$ is the initial order parameter at $t = 0$, and $S_\infty = (U-1)/U$ is the stationary value for infinite t. The integral $I = \int G\, dt$ is the total strain the surface layer undergoes.

To compare the theoretical values of the order parameter S as a function of the total deformation (eq 3.17) with the experimental results indicated in Figure 19, where S is plotted versus the emersion length of the substrate, it has been assumed that the velocity profile within the convergent zone advances parallel toward the substrate. The strain can then be estimated from the convergent streamlines.

For the fit indicated in Figure 19, the chosen parameters are as follows: $S_0 = -0.1$, which is an experimentally observed starting value; $S_\infty = 0.5$ slightly higher than typical values for multilayers of PcPS, i.e., $U = 2$; and a flow field correction factor $m = 1.5$.

As shown in Figure 19, there is a large difference between the experimental results and the theoretically estimated values. In fact, the major deviation is due to an experimentally found "induction" period, where the order parameter is unaffected. This "induction" period is discussed in terms of two sets of arguments:

The first is due to necessary simplifications: From the theoretical viewpoint, the stream has been regarded as

fully developed right from the beginning of transfer. But during the building up (first deposition area on the substrate) the stream may be different from the converging flow pattern, although an "induction" period on the substrate of 1.5 cm, which means ~0.5-cm movement of the monolayer on the water subphase, seems to be very large for this building-up process. Nevertheless, if the fit curve is shifted along the x-axis, the agreement with the experimental results is satisfying (Figure 19, dashed line). But the fact should not be overestimated, because eq 3.17 neglects diffusion and the polydispersity of the investigated PcPS. Polydispersity certainly influences the deformation-induced orientation. It is known that low molecular weight nematics and high molecular nematics show a different behavior in shear flow.[27]

The second is for fundamental reasons: If the macroscopic orientation cannot be described by the orientation of the molecules but of assemblies of molecules (domains) during the deformation of the monolayer, a behavior differing from the theory can be expected. There is evidence for molecular aggregates even in the "expanded" state (π = 0) for PG and PcPS[35] to form island-like structures, but this point is currently under investigation.

4. Orientation Process at and after Deposition

So far the macroscopic orientation originated by the flow and deformation of monolayers consisting of rigid-rod polymers has been discussed by neglecting the possible effect of the force field at the meniscus. This seems to be justified by the obvious relationship between convergent flow and molecular orientation as seen before. A detailed discussion of the meniscus effect with respect to the studied polymers is presented in this section.

The transfer mechanism of fatty acid monolayers has been studied both theoretically and experimentally by several authors.[36-39]

Direct force measurements at the substrate during the up and down stroke through the air–monolayer–water interface allow the determination of the dynamic forces of immersion and emersion. For the desired purpose these forces have to be correlated with the deformation (elongation) of the monolayer at the meniscus to estimate the possible orientation effect.

4.1. Estimation of the Shear Force Acting on the Monolayer. The force balance during the emersion process of a substrate can be written as

$$F = F_g - F_b + \gamma p \cos \chi_{em} \tag{4.1}$$

where F is the total force, F_g and F_b are the gravity and the buoyancy forces of the substrate, respectively, γ is the surface tension, p is the perimeter of the substrate, and χ_{em} is the contact angle during emersion.

The interfacial force of the emersion process is

$$f_{em} = \gamma \cos \chi_{em} \tag{4.2}$$

A similar equation can be given for the interfacial force of the immersion process:

$$f_{im} = \gamma \cos \chi_{im} \tag{4.3}$$

The difference Δf of the interfacial force in the dynamic process of transfer and in equilibrium without substrate movement is

$$\Delta f = (\gamma \cos \chi)_d - (\gamma \cos \chi)_e \tag{4.4}$$

where d and e indicate the dynamic and equilibrated value of the interfacial force, respectively. This force difference may be assigned to dissipation of macroscopic flow in the meniscus and can then be interpreted as a hydrodynamic force.[39]

$$\Delta f = f'_h \tag{4.5}$$

where f'_h is the force in the case of monolayer transfer and the prime is used to indicate that this force is different from the hydrodynamic force f_h responsible for the deformation of the monolayer (see below).

To estimate the force field at the meniscus, the stream function Ψ has to be evaluated. This problem has been analyzed in a classical paper by Huh and Scriven.[39]

In the two-dimensional creeping flow approximation of a Newtonian fluid the Navier–Stokes equation leads to a biharmonic equation for the stream function:

$$\nabla_2^4 \Psi = 0 \tag{4.6}$$

The general solution of eq 4.6 in plane polar coordinates is

$$\Psi(r,\theta) = r^{-1}(a \sin \theta + b \cos \theta + c\theta \sin \theta + d\theta \cos \theta) \tag{4.7}$$

The boundary conditions to be imposed are shown in Figure 21.

1. No normal velocity component at the solid surface and the liquid–layer interface.

$$v_\theta = \frac{\partial \Psi}{\partial r} = 0 \qquad \text{at } |\mathbf{r}| = r \geq 0, \theta = 0 \text{ or } \theta = \chi \tag{4.8}$$

where $\mathbf{r}$ is the vector of the investigated point in a coordinate system with its origin at the "three-phase" contact and θ is the angle between $\mathbf{r}$ and the solid surface.

2. No slipping at the solid surface.

$$v_r = -\frac{1}{r}\frac{\partial \Psi}{\partial \theta} = v_d \qquad \text{at } \mathbf{r} > 0, \theta = 0 \tag{4.9}$$

3. The film has the same speed as the substrate.

$$v_r = v_d \qquad \text{at } r \geq 0, \theta = \chi \tag{4.10}$$

Equation 4.10 is of course a rough approximation. But it should be useful if the elongation is small. With the present boundary conditions, the constants of eq 4.7 have found to be[37]

$$a = \frac{\chi v_d}{\sin \chi - \chi} = a' f_d \qquad b = 0$$

$$c = \frac{v_d(\cos \chi - 1)}{\sin \chi - \chi} = c' v_d \qquad d = \frac{v_d \sin \chi}{\sin \chi - \chi} = d' v_d \tag{4.11}$$

With the stream function Ψ the shear stress on the monofilm can be determined:

$$T_{r\chi} = \eta \left.\frac{\partial^2 \Psi}{\partial \theta^2}\right|_{\theta=\chi} = \frac{\eta v_d}{r} f(\chi) \tag{4.12}$$

where

$$f(\chi) = -(a' + 2d') \sin \chi + 2c' \cos \chi - c'\chi \sin \chi - d'\chi \cos \chi \tag{4.13}$$

η is the viscosity of water, and a', c', and d' are defined in eq 4.11.

The shear force on the monofilm at the meniscus is calculated by integration along the meniscus:

$$f_h = \int_{r_{min}}^{r_{max}} T_{r\chi}\, dr = \eta v_d f(\chi) \ln r \Big|_{r_{max}}^{r_{min}} \tag{4.14}$$

where r_{min} should be of a molecular size and r_{max} should be in the range of the capillary length. The value of ln (r_{max}/r_{min}) has been estimated by de Gennes as 12.[40]

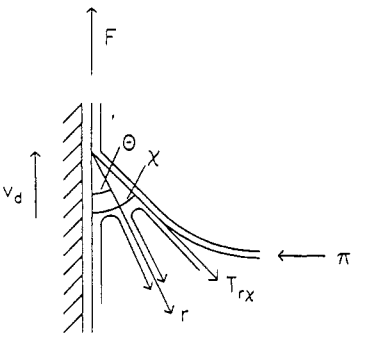

Figure 21. Boundary conditions for the LB transfer process of a monolayer during emersion: χ contact angle; v_d dipping velocity; π applied surface pressure; for T_{rx}, r, Θ, see text.

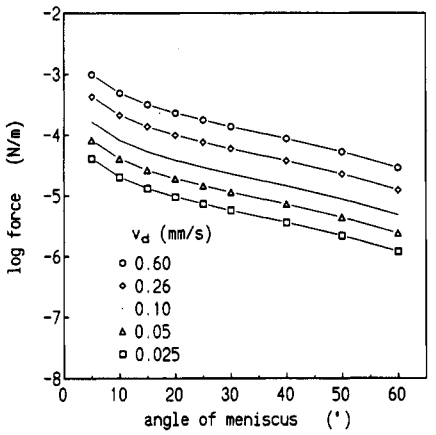

Figure 22. Calculated hydrodynamic force for the emersion process during LB transfer as a function of the contact angle: parameter, v_d.

Now the hydrodynamic force under the experimental conditions can be calculated using eq 4.14. The results, in Figure 22, show that the interfacial force should strongly depend on the contact angle and that it is proportional to the dipping velocity.

This shear force acting on the monofilm will presumably cause some elongation of the monolayer near the three-phase line. But before this elongation is estimated, the theoretical force calculation should be compared with the experimental results.

4.2. Measurement of Dynamic and Static Forces. A direct force measurement during the transfer process has already been made in the case of fatty acids.[38,41]

In the present investigation, a sensitive force transducer was mounted between the lift and the substrate which allows the measurement in the range of 0.5 N with a resolution of $\pm 10^{-5}$ N.

A typical force trace during one dipping cycle (immersion and emersion) is shown in Figure 23. The forces indicated in this figure and their values, after division by the perimeter, given in Table II are the dynamic force of immersion $-f_{im}$, the dynamic force of emersion f_{em}, and the force due to the change of the meniscus switching the substrate movement from immersion to emersion f_2, which should approximately equal the sum of the immersion and emersion forces. The force values have been corrected regarding the buoyancy change of the substrate (see Figure 23).

The difference of the dynamic and the static interfacial forces, i.e., the hydrodynamic force, has been measured directly by the force deviation after lift stop (see Figure 23). It should be noted that the obtained values are the sum of the forces acting on both walls of the contact angle ($\chi = 0$ and $\chi = \theta$; see Figure 21). Therefore, the symbol

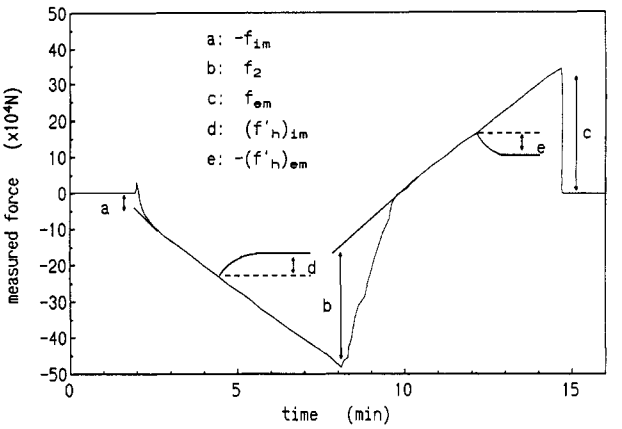

Figure 23. Measured forces during one dipping cycle for the two-sided transfer of PcPS on a substrate coated with PcPS: substrate perimeter 54 mm; T = 6 °C; π = 25 mN/m; v_d = 0.3 cm/min.

f'_h is used rather than f_h (as for the theoretical value), where $f'_h = (1 + \cos \chi) f_h$.

The data were found to be severely affected by surface roughness or contaminations. Therefore, the values in Table II are averaged.

The interest of the present investigation is focused on the hydrodynamic force. Therefore, the experimental data will be compared to eq 4.13:

1. The forces $(f'_h)_{im/em}$ increase as the deposition velocity increases but less than proportionally as theoretically predicted for the hydrodynamic force.

2. The f'_h forces are comparable for the dipping process with or without monolayer deposition, opposite to the theoretical prediction.[39]

3. The experimental $-(f'_h)_{em}$ values of PcPS and PG are similar and range in the order of 1 mN/m. To compare this result with the estimated dissipation force, the contact angle for the emersion process has to be known. It has been determined by simple observation of the "three-phase" line during the upstroke and is ~40°, only slightly depending on the dipping velocity. This value is a little smaller than typical contact angles for fatty acid monolayers.[38] The theoretical predicted dissipation force is then in the range of 10^{-4} N/m and, therefore, at least 1 order of magnitude lower than the experimental results. But it has to be admitted that the contact angle directly at the three-phase line, which dominates the force, may be smaller than the observed one.

Regarding the deviation between the theoretical calculation and the experimental results, it has to be remembered that the idealizations made in the theory are very crude for the polymer systems under investigation. For example, PcPS and PG show a non-Newtonian behavior in their flow patterns. Therefore, viscous dissipation seems to play an important role for the dynamic process but other effects might also influence the results.

4.3. Film Elongation at the Meniscus. First, it should be remembered that the maximum value of the drawing force is on the order of 10 mN/m and therefore smaller than the applied surface pressure. The deformation of the monolayer during deposition can then be regarded as an elongation of a compressed monolayer. To estimate the elongational strain ϵ, which is defined as

$$\epsilon = f/E \tag{4.15}$$

the elongational force f and the two-dimensional modulus E have to be determined. The upper limit of the elongational force f is on the order of 10 mN/m, as shown in section 4.2. The modulus E is roughly estimated to equal

Table II
Forces of Immersion and Emersion during the Deposition Process

"transferred" phase	sublayer	π, mN/m	T, °C	velocity v_d, mm/s	forces,[c] mN/m $-f_{im}$	f_2	f_{em}	$(f'_h)_{im}$	$-(f'_h)_{em}$
PcPS	PcPS	25	6	0.05	7	54	57	3	6
		25	6	0.26	9	61	58	7	9
		25	6	0.60	13	66	60	10	11
	glass[a]	25	6	0.05	20	77	57[b]		
PG	PG[c]	19	20	0.05	3	47	48		4
		19	20	0.26			50		6
		19	20	0.60			51		8
	glass[a]	19	20	0.05	8	52	52[b]		
water	PcPS		6	0.05	15	39	31	6	5
	PG		20	0.05	3	47	54	4	4
	glass[a]		6	0.05	3	35	41	6	3
			6	0.26	4	37	41	7	5
			6	0.60	9	41	41	9	7

[a] Glass plate hydrophobized by treatment with hexamethyldisilazane. [b] f_{em} is measured for the transfer of a monolayer onto a substrate covered with one monolayer of the same material. [c] f-Values cannot be given completely due to unsteady movement of the contact line (irregular jumps).

Table III
Estimated Values of Modulus E and Strain ϵ

	polymer			
	PcPS	PG	i-PC	n-BC
E, mN/m	240	88	98	108
ϵ, %	4	11	10	9

the compression modulus measured from the slope of the isotherm in the π/A diagram (Figure 12):

$$E = \Delta\pi/(\Delta A/A) \tag{4.16}$$

Assuming that this modulus determines the elongational strain at the meniscus, ϵ can be estimated as shown in Table III.

Remember that the stress concentrates near the three-phase line and so does the strain. The resulting elongation seems to be too small to create any noticeable orientation in the monolayer.

On the other hand the strain together with the elongational stress might be frozen in during deposition of the monolayer. This might be one reason for the observed relaxation process in the supramolecular structure of PcPS at elevated temperatures, which will be discussed in the next chapter.

4.4. Postorientation during Annealing. According to the experimental results described in section 3.2.3, the relaxation time of the macroscopic orientation at the air–water interface is very long under the operating conditions in the case of PcPS, and therefore, it could be expected that the mobility of the main chains in the layered assemblies is frozen at room temperature.

When the temperature rises to 100 °C and higher, however, the side chains of PcPS become very mobile and further changes of orientation are observed. Figure 24 shows that the order parameter increases with time upon heating at various temperatures in an argon atmosphere. If carefully prepared samples with similar initial orientations are investigated, the time dependence of the order parameter at different temperatures can be plotted as a function of a reduced time $a_T t$; i.e., all curves can be superimposed to a master curve (Figure 25). Here a_T is the shift factor. Knowing a_T, the postorientation can be predicted at any given temperature. The existence of a master curve reveals that the physical mechanism for the orientation is the same at all temperatures. The driving force of this process could be twofold: First, the layered assembly as prepared contains free volume, which is annealed out increasing the dense alignment of the rodlike

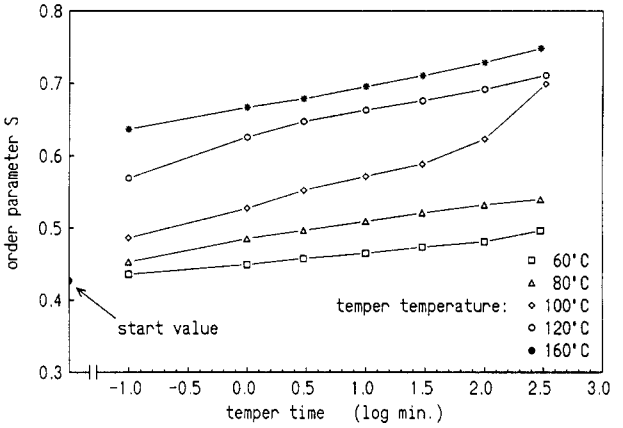

Figure 24. Development of the order parameter S of 40 layers of PcPS during annealing: parameter, T.

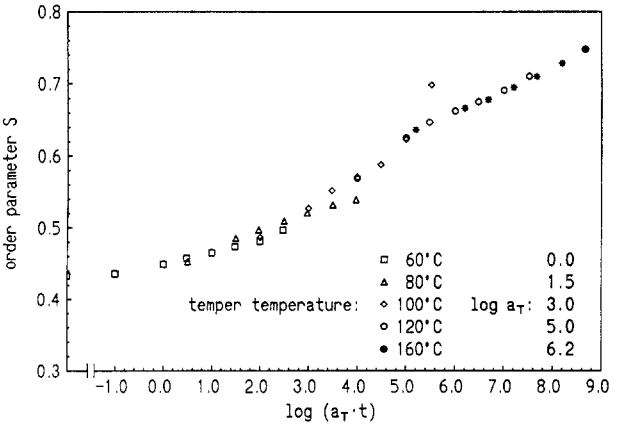

Figure 25. Order parameter S as a function of the reduced time $a_T t$ for the annealing process of 40 layers of PcPS.

entities; second, the layered assembly has stored internal stress as a consequence of misalignments of the molecular entities during the deposition process. The contributions of the two factors need further investigations.

5. Concluding Remarks

1. The flow fields of PcPS, PG, i-PC, and n-BC on the water surface have been determined by a flow visualization method. Monolayers of PcPS and PG show a viscoplastic behavior, while i-PC and n-BC exhibit flow patterns like viscoelastic fluids. For a realistic flow modeling, the condition of a slipping boundary should be used.

2. The macroscopic orientation in the monolayer has been determined by polarized spectroscopy after transfer

onto a solid substrate. This orientation can be correlated to the deformation of the plane elements during convergent flow. The necessity of deformation to obtain a macroscopic orientation has been shown for several transfer geometries.

The relaxation of this deformation-induced orientation is rather slow, and therefore, the order parameter is almost independent of the transfer velocity.

3. The development of macroscopic orientation has been approximated by the model of a two-dimensional, nematic liquid crystal suffering shear. The equation of orientation evolution has been obtained based on the transient solution of this model. Deviations between the theoretical values and the experimental results have been discussed.

4. The difference between the dynamic and static interfacial force at the meniscus has been measured and compared to a calculation based on a model of viscous dissipation. The upper limit of the shear force on the monofilm at the meniscus has been estimated to be on the order of 10 mN/m. Therefore, the corresponding molecular orientation is negligible compared to the deformation-induced orientation on the water surface.

5. The order parameter S of the deposited multilayer of PcPS has been enhanced at elevated temperatures. This process obeys the time–temperature superposition principle.

Acknowledgment. This work was supported by the Materialforschungsprogramm des Bundesministers für Forschung und Technologie under the project "Ultradünne Schichten". Financial support for Y.X. by the A. v. H. foundation and for T.V. by the Verband der chemischen Industrie is gratefully acknowledged. Thanks are also due to Dr. L. Brombacher and to F. Embs, K. Mathauer, and Dr. M. Reidy for the supply of polymer and spectroscopic measurements.

References and Notes

(1) Gorter, E.; Grendel, F. *Proc. K. Akad. Wet. Amsterdam* **1925**, *29*, 371; *Trans. Faraday Soc.* **1926**, *22*, 477.
(2) Wegner, G. *Adv. Mater.* **1991**, *3*, 8.
(3) Fuchs, H.; Ohst, H.; Prass, W. *Adv. Mater.* **1991**, *3*, 10.
(4) Embs, F.; Funhoff, D.; Laschewsky, A.; Licht, U.; Ohst, H.; Prass, W.; Ringsdorf, H.; Wegner, G.; Wehrmann, R. *Adv. Mater.* **1991**, *3*, 25.
(5) Orthmann, E.; Wegner, G. *Angew. Chem.* **1986**, *98*, 1114; *Angew. Chem., Int. Ed. Engl.* **1986**, *25*, 1105.
(6) Duda, G.; Shouten, A. J.; Arndt, T.; Lieser, G.; Schmidt, G. F.; Bubeck, C.; Wegner, G. *Thin Solid Films* **1988**, *159*, 221. Duda, G.; Wegner, G. *Makromol. Chem., Rapid Commun.* **1988**, *9*, 496.
(7) Hickel, W.; Duda, G.; Jurich, M.; Kröhl, T.; Rochford, K.; Stegemann, G. I.; Swalen, J. D.; Wegner, G.; Knoll, W. *Langmuir* **1990**, *6*, 1403.
(8) Sauer, T.; Arndt, T.; Batchelder, D. N.; Kalachev, A. A.; Wegner, G. *Thin Solid Films* **1990**, *187*, 357.
(9) Roberts, G. *Langmuir Blodgett Films*; Plenum Press: New York, 1990.
(10) Sauer, T.; Caseri, W.; Wegner, G.; Vogel, A.; Hoffmann, B. *J. Phys. D: Appl. Phys.* **1990**, *23*, 79.
(11) Caseri, W.; Sauer, T.; Wegner, G. *Makromol. Chem., Rapid Commun.* **1988**, *9*, 651.
(12) Mathauer, K. Ph.D. Thesis, Mainz, 1991.
(13) Ritcey, A. M.; Wenz, G. *Makromol. Chem.*, to be published.
(14) Minari, N.; Ikegami, K.; Kuroda, S.; Saito, K.; Saito, M.; Sugi, M. *J. Phys. Soc. Jpn.* **1989**, *58*(1), 222.
(15) Streeter, V. L., Ed. *Handbook of Fluid Dynamics*; Mc Graw-Hill, New York, 1961.
(16) IMSL, Version 2.0, 2, 688, IMSL Inc., 1987.
(17) Crochet, M. J.; Davies, A. R.; Walters, K. *Numerical Simulation of Non-Newtonian Flow*; Elsevier: Amsterdam, 1984.
(18) Keunings, R.; Crochet, M. J. *J. Non-Newtonian Fluid Mech.* **1984**, *14*, 279.
(19) Determined for ethylcellulose: Yamakawa, H. *Modern Theory of Polymer Solutions*; Harper & Row: New York, 1971.
(20) Miller, L. S.; Hookes, D. E.; Travers, P. J.; Murphy, A. P. *J. Phys. E: Sci. Instrum.* **1988**, *21*, 163.
(21) Daniel, M. F.; Hart, J. T. T. *J. Mol. Electron.* **1985**, *1*, 97.
(22) Walters, K.; et al. *J. Non-Newtonian Fluid Mech.* **1977**, *2*, 191; **1979**, *4*, 325; **1979**, *5*, 113; **1981**, *8*, 95.
(23) White, S. A.; Baird, D. G. *J. Non-Newtonian Fluid Mech.* **1988**, *29*, 245.
(24) Ericksen, J. L. *Phys. Fluids* **1966**, *9*, 1205.
(25) Leslie, F. M. *Arch. Ration. Mech. Anal.* **1968**, *28*, 265.
(26) de Gennes, P. G. *The Physics of Liquid Crystals*; Oxford University Press: New York, 1974.
(27) Doi, M.; Edwards, S. F. *The Theory of Polymer Dynamics*; Clarendon Press: Oxford, UK, 1986.
(28) Sauer, T.; Caseri, W.; Wegner, G. *Mol. Cryst. Liq. Cryst.* **1990**, *183*, 387.
(29) Arndt, T. Ph.D. Thesis, Mainz, 1989.
(30) Marrucci, G.; Maffettone, P. L. *Macromolecules* **1989**, *22*, 4076.
(31) We are aware of an earlier publication by Tredgold and Jones in which they describe orientational phenomena during the transfer of poly(γ-benzyl L-glutamate) to solid substrates by the Schaefer technique: Jones, R.; Tredgold, R. H. *J. Phys. D: Appl. Phys.* **1988**, *21*, 449. In light of our investigation on the relationship between experimental parameters (trough width versus substrate width, etc.), we are forced to assume that the phenomena observed by these authors are a consequence of the rather special conditions of their experiment.
(32) Embs, F. Ph.D. Thesis, Mainz, 1991.
(33) Ogawa, K.; Yonehara, H.; Shoji, T.; Kinoshita, S.; Maekawa, E. *Thin Solid Films* **1989**, *178*, 439.
(34) Doi, M. *J. Polym. Sci., Polym. Phys. Ed.* **1981**, *19*, 229.
(35) Yase, K.; Schwiegk, S.; Wegner, G. in preparation.
(36) Petrov, J. G.; Kuhn, H.; Möbius, D. *J. Colloid Interface Sci.* **1980**, *73*, 66.
(37) Egusa, S.; Gemma, N.; Azuma, M. *J. Phys. Chem.* **1990**, *94*, 2512.
(38) Buhaenko, M. R.; Richardson, R. M. *Thin Solid Films* **1988**, *159*, 231.
(39) Huh, C.; Scriven, L. E. *J. Colloid Interface Sci.* **1971**, *35*, 85.
(40) de Gennes, P. G. *Colloid Polym. Sci.* **1986**, *264*, 463.
(41) Peng, J. B.; Abraham, B. M.; Dutta, P.; Ketterson, J. B. *Thin Solid Films* **1985**, *134*, 187.

Registry No. PG (copolymer), 83789-62-2; *i*-PC, 139630-75-4; *n*-BC, 56729-14-7.